Icarus 316 (2018) 154–166

Contents lists available at ScienceDirect

Icarus

journal homepage: www.elsevier.com/locate/icarus

Geologic mapping of the Ac-11 Sintana quadrangle: Assessing diverse crater morphologies

F. Schulzeck[a,*], K. Krohn[a], I. v.d. Gathen[a], N. Schmedemann[b], K. Stephan[a], R. Jaumann[a], D.A. Williams[c], R. Wagner[a], D.L. Buczkowski[d], S.C. Mest[e], J.E.C. Scully[f], E. Kersten[a], K.-D. Matz[a], A. Naß[a], F. Preusker[a], T. Roatsch[a], C.A. Raymond[f], C.T. Russell[g]

[a] German Aerospace Center (DLR), Rutherfordstrasse 2, 12489 Berlin, Germany
[b] Freie Universität Berlin, Berlin, Germany
[c] School of Earth & Space Exploration, Arizona State University, Tempe, AZ, USA
[d] JHU-APL, Laurel, MD, USA
[e] Planetary Science Institute, Tucson, AZ, USA
[f] Jet Propulsion Laboratory, California Institute of Technology, Pasadena, CA, USA
[g] UCLA, Los Angeles, CA, USA

ARTICLE INFO

Article history:
Received 8 August 2016
Revised 22 November 2017
Accepted 7 December 2017
Available online 11 December 2017

ABSTRACT

A geologic map at a scale of 1:1,000,000 of the Ac-11 Sintana quadrangle (21–66°S and 0–90°E) from the dwarf planet Ceres and based on data from NASA's Dawn spacecraft, was produced as part of a geologic mapping campaign in order to investigate the surface structure, stratigraphy, composition and surface modifying processes. The Sintana quadrangle is geologically dominated by cratered terrain with morphologically distinct crater types. The most prominent craters, Sintana, Hamori, Jarimba, Tupo, Annona and Darzamat, have complex structures including smooth crater material covering their floors, collapsed crater walls forming terraces, and central ridges. Multiple gravity-driven blocky mass wasting features indicate post-impact crater modification and are indicative of an ice-rich subsurface, in which there is no topographic or structural evidence of endogenic activity visible in the quadrangle. Absolute age estimates suggest that the entire surface in the quadrangle was resurfaced ~1.1 Ga ago, possibly by Kerwan-related impact-induced melting.

1. Introduction and geologic setting

Launched in September 2007, NASA's Dawn spacecraft arrived at the dwarf planet Ceres on March 6, 2015, with the goal to investigate the largest massive body in the asteroid belt in order to understand its origin, evolution, composition and the variety of geologic processes that were active in the early Solar System (McCord and Sotin, 2005; Russell and Raymond, 2011). A combined approach of gravitational studies (Konopliv et al., 2011), visible and near-infrared spectroscopic measurements (De Sanctis et al., 2011), gamma-ray and neutron spectroscopy (Prettyman et al., 2011) and photogeologic and topographic analysis with Dawn's framing camera (Sierks et al., 2011) was used to study Ceres.

Both new data and models are used to refine our knowledge about Ceres' interior and shape. Recent Dawn-based gravity models describe Ceres as a partially differentiated body with a rocky core (Ermakov et al., 2017; Park et al., 2016). Pre-Dawn models suggested a pure water-ice shell for Ceres and hence predicted a sparsely cratered surface due to viscous relaxation (Bland, 2013; Castillo-Rogez and McCord, 2010; McCord and Sotin, 2005), instead Dawn observed a heavily cratered surface (Buczkowski et al., 2016; Hiesinger et al., 2016). Pristine crater morphologies and Dawn-derived shape and gravity models indicate a strong crust and suggest a rock–ice mixture with less than 40% ice instead of a pure water-ice shell (Bland et al., 2016; Fu et al., 2017; Hiesinger et al., 2016; Park et al., 2016). Viscous relaxation is found to be only relevant for scales of several hundreds of kilometers, such as for the partially relaxed Kerwan crater (284 km) (Fu et al., 2017; Hiesinger et al., 2016; Williams et al., 2017b, this issue).

Ceres' global geology is dominated by impact craters as the most ubiquitous surface features (Hiesinger et al., 2016), with a variety of shapes and structures, such as polygonal craters, floor-fractures, terraces, central peaks, smooth crater floors, flow-like features, mounds and central pits (Buczkowski et al., 2016). Morphologies of craters with diameters up to 30-40 km

* Corresponding author.
E-mail address: franziska.schulzeck@dlr.de (F. Schulzeck).

https://doi.org/10.1016/j.icarus.2017.12.007
0019-1035/

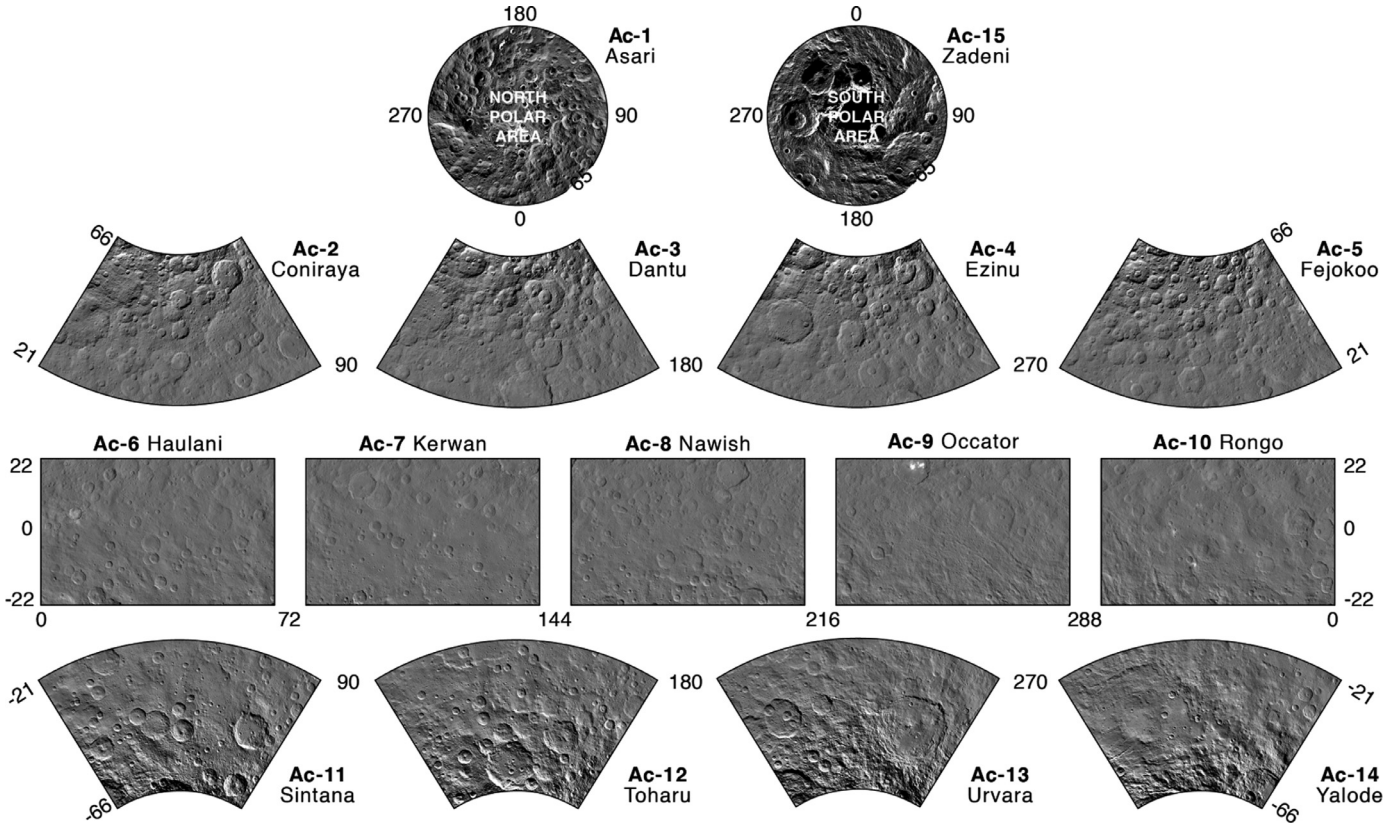

Fig. 1. Cartographic scheme of 15 quadrangles used for HAMO- and LAMO-based regional geologic mapping (Roatsch et al., 2016).

are remarkably similar to those on icy satellites in the outer Solar System (Hiesinger et al., 2016; Schenk et al., 2016). Hiesinger et al. (2016) found that the transition from fresh simple-bowl shaped craters to modified complex craters occurs at 7.5–12 km. On Ceres, craters larger than 300 km are absent (Hiesinger et al., 2016), suggestive of a geologically young surface.

The Dawn Science Team established a geologic mapping campaign for Ceres, similar to that undertaken for the asteroid Vesta (Williams et al., 2014; Yingst et al., 2014), in order to assess the geological history of Ceres. A series of 15 quadrangle geologic maps (Fig. 1) provides geologic context information for the analysis of surface features observed in Framing Camera images as the baseline for further investigations and models.

The Ac-11 Sintana quadrangle, which is named after one of its prominent impact craters Sintana, is located in Ceres' southern hemisphere between 21-66°S and 0–90°E. In addition to providing an overview of the main geologic units in the area of the Sintana quadrangle, major goals of this work are (1) the investigation of the diversity of crater morphologies and the progression from a recently emplaced to a geologically old degraded impact feature. (2) The southern hemisphere of Ceres is less heavily cratered than its northern hemisphere, because of resurfacing caused by large impacts such as Kerwan, Urvara and Yalode (Hiesinger et al., 2016; Marchi et al., 2016). Therefore, we use a combination of geologic mapping and crater size frequency distribution (CSFD) measurements to look for evidence of resurfacing either by impact ejecta emplacement or internal activities.

2. Data and methodology

We used Dawn Framing Camera (FC) data sets of different spatial resolutions to obtain a comprehensive understanding of the study area. For a more detailed description of the Dawn mapping approach, we refer readers to the introductory paper of this issue by Williams et al. (2017a, this issue). Clear filter mosaics based on Dawn Framing Camera images (Sierks et al., 2011) are the primary base for mapping. The Dawn Framing Camera (FC) data sets that have been acquired during different phases of the Dawn mission are: Survey Orbit (415 m/pixel), High Altitude Mapping Orbit (HAMO, 140 m/pixel) and Low Altitude Mapping Orbit (LAMO, 35 m/pixel) (Roatsch et al., 2016). The final geologic map used an uncontrolled LAMO clear filter mosaic (Fig. 2). Information about the albedo is based on photometrically corrected clear filter images.

Furthermore, HAMO FC clear filter images have been used to produce a stereophotogrammetry-based digital terrain model (DTM) (Fig. 3) (Preusker et al., 2016), which enables the assessment of the topography in the quadrangle. It also allows for the determination of slopes and profiles that are used for relative steepness analyses.

In addition, images acquired in the seven color filters of the FC camera provide spectral information and support the investigation of relationships between stratigraphy and composition. We use the ratio of the filters F8 (438 nm) and F3 (749 nm), which have been identified as a useful additional tool in roughly estimating relative surface ages by weathering related spectral alteration of surface materials (Schmedemann et al., 2016; Stephan et al., 2017a). Ratio values are directly correlated to the visible spectral slope, which particularly can indicate differences in the chemical, but mostly in the physical surface properties (Stephan et al., 2017b). Ratio values <1 indicate a positive ('red') spectral slope and ratio values >1 point to a negative (blue) spectral slope (Stephan et al., 2017a). The values of the two photometrically corrected color filters are divided on a pixel-by-pixel basis. We applied a median filter of 8 by 8 pixels onto the resulting ratio image, which reduces the image resolution by a factor 8, but considerably improves the signal-

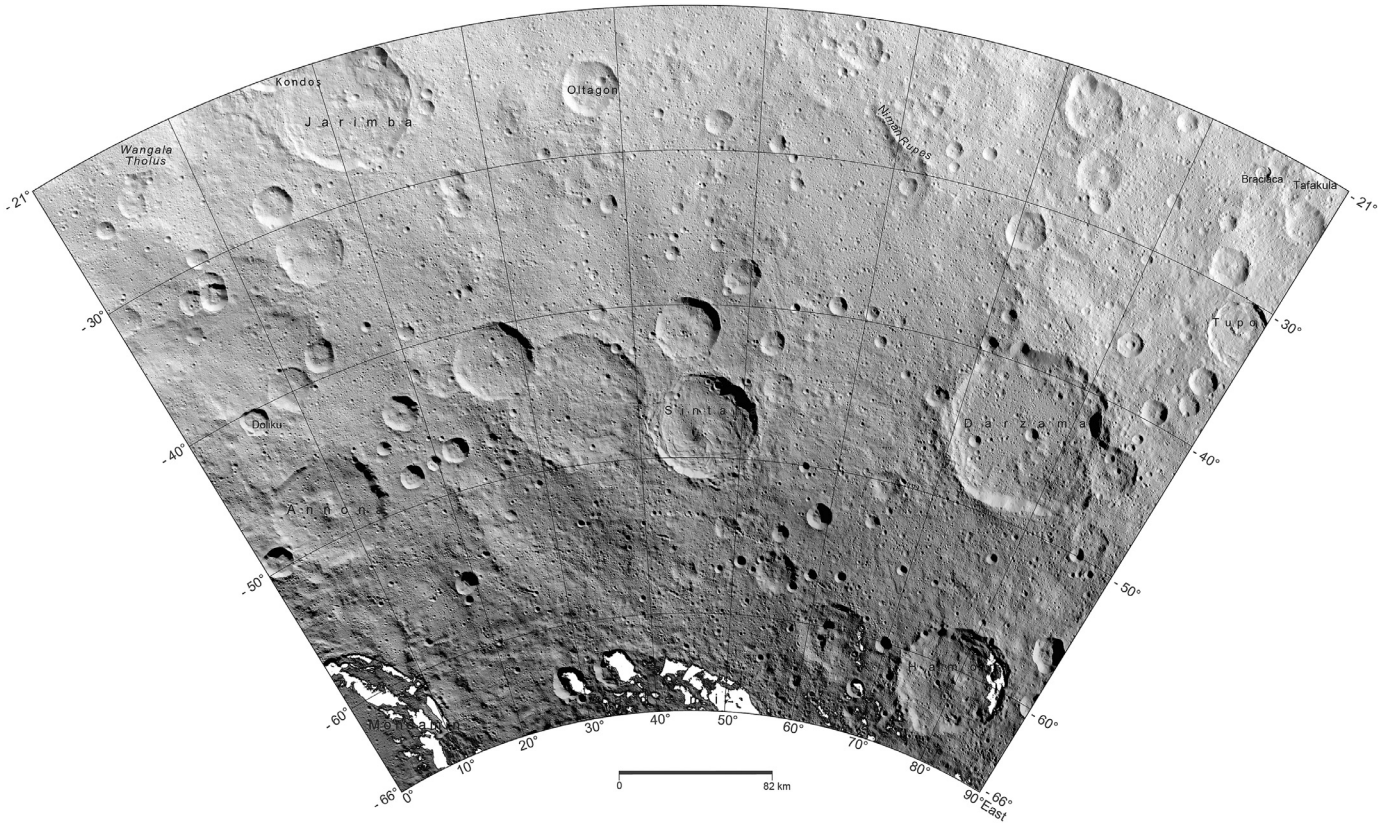

Fig. 2. Dawn FC clear filter mosaic of the Ac-11 Sintana quadrangle.

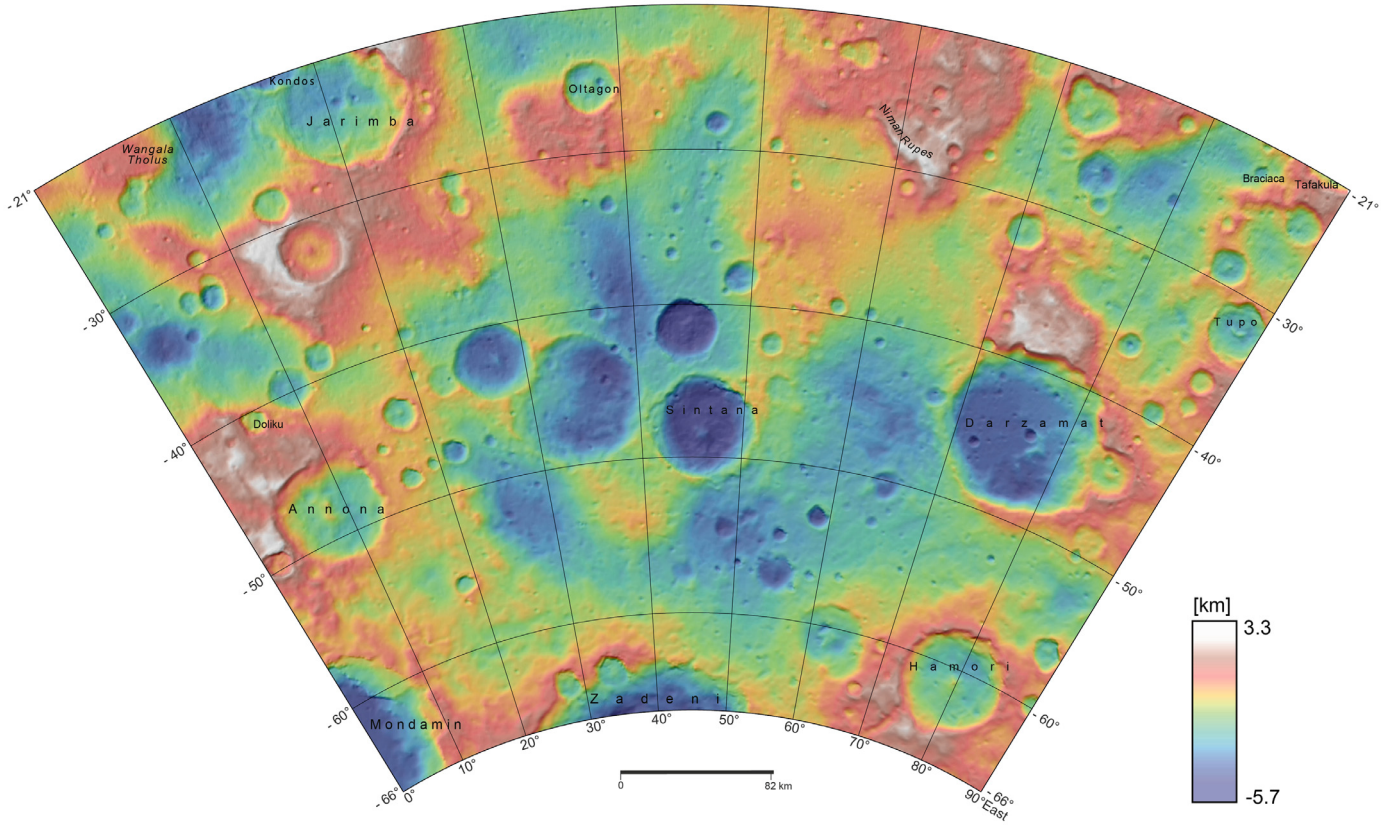

Fig. 3. HAMO-based digital terrain model (50% transparency) derived from Dawn Framing Camera images on top of a hillshade. The variation in topography is about 9 km.

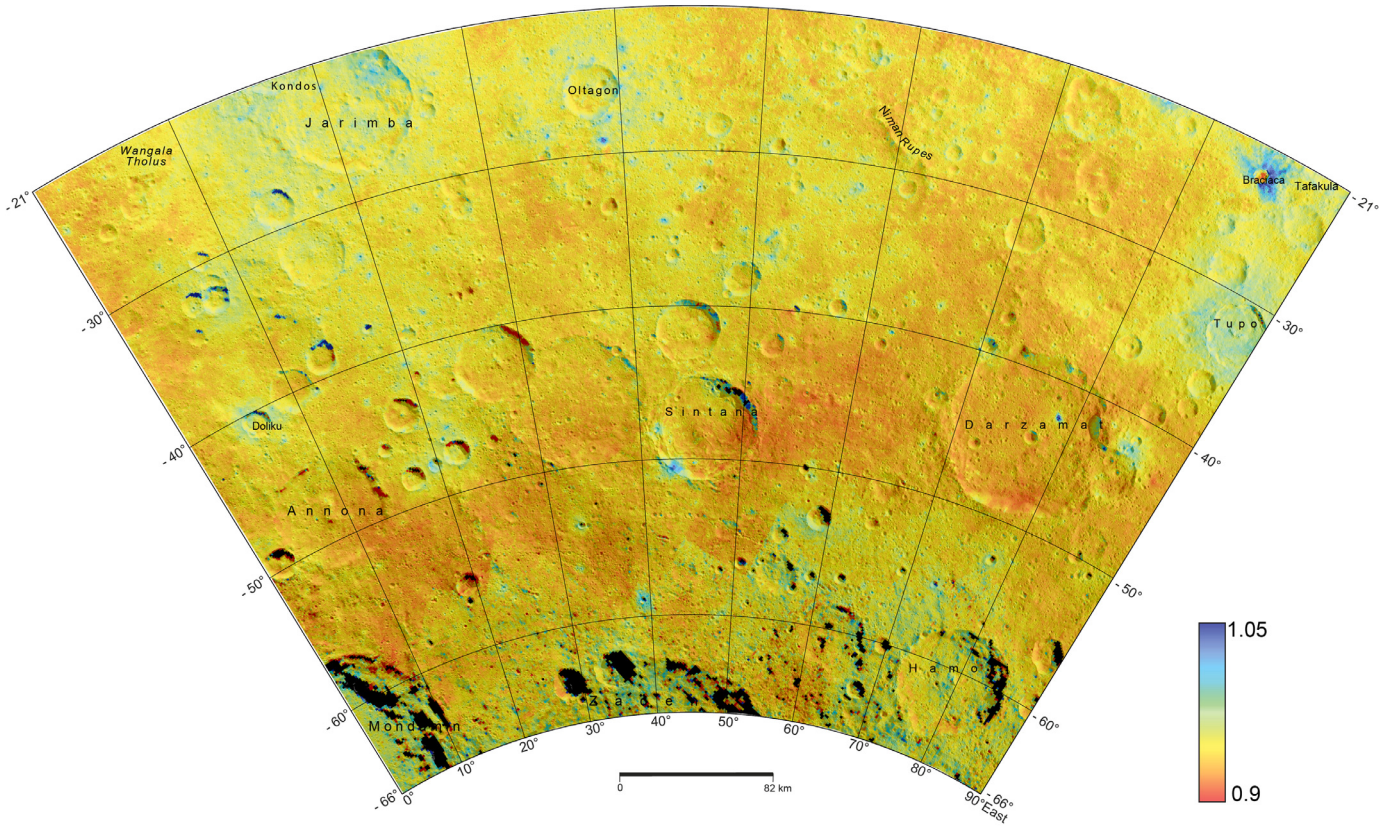

Fig. 4. Color ratio F8 (438 nm)/F3 (749 nm) displayed with a transparency of 40% on a hillshade.

to-noise ratio (SNR) and provides a high quality ratio image sufficient for our analysis. The resulting color-coded ratio map (Fig. 4) shows variations in the resulting ratio values between 0.9 and 1.05 throughout the Sintana region, implying changes from a reddish to a bluish visible spectral slope between 438 and 749 nm.

The geologic mapping was performed within the Esri's ArcGIS Suite (release 10.3). An ArcGIS mapping template (Naß et al., 2015) that provides the standardized cartographic symbols for planetary mapping (Naß et al., 2011) based on the FDGC Digital Cartographic Standard for Geologic Map Symbolization (USGS, 2006) was used by the mapping team. The final map scale is 1:1,000,000, while the detailed geologic mapping was conducted at a higher scale of 1:100,000. Individual features such as the diameter of craters or the length of linear structures and polygonal sides were mapped down to a size of 5 km. The mapping accuracy of the boundaries of single structures ranges from several tens of meters to a few hundred meters, dependent on the sharpness of individual contacts.

Crater size frequency distributions (CSFD) were used to support relative age estimation of geologic units. The CSFD is measured with the standardized approach described in Kneissl et al. (2011) using the CraterTools extension for Esri's ArcMap. This program minimizes distortion effects on account of different map projections. Crater modeling ages are then determined using the CraterStats software (Michael, 2013; Michael and Neukum, 2010) by fitting the observed CSFD to the production function. The production function (PF) can then be used to derive crater model ages from the chronology function (CF). Two types of production function and chronological model ages are used for Ceres: the lunar-derived model (LDM), which adapts lunar CF and PF to Cerean impact conditions as well as the asteroid-derived model (ADM) (Hiesinger et al., 2016). For our study, results from both chronology systems are reported. For the cratered terrain, only craters larger than 5 km were included to avoid secondary craters whose diameters usually are below 5 km. The maximum size of secondary craters is usually 5% of the size of their primary crater (e.g. Shoemaker, 1965). Using craters larger than 5 km will avoid most secondaries, but still allows the inclusion of as many craters as possible. In addition, randomness analyses (Michael et al., 2012) were applied to test for clustering with secondary craters. We used the M2CND (Mean 2nd-closest neighbor distance) as the measure for spatial configuration. It descibes the distribution of the real data and randomly distributed configurations generated by a Monte Carlo simulation via various iterations. The result is a histogram describing the relative likelihoods of derived values.

3. Results

3.1. Topography and structural features

The DTM of the Ac-11 Sintana quadrangle shows an undulating surface with topographic variations ranging over ~9 km, with a minimum at −5.7 km and a maximum at 3.2 km. An extended depression, with its center near the impact crater Sintana, characterizes major portions of the cratered terrain. This depression is part of an impact basin planitia C (~500 km in diameter) postulated by Marchi et al. (2016) based on the investigation of long wavelength topography. The quadrangle region is also characterized by several local regions of high topography (Fig. 3) that are mapped as topographic rises. The positive topographic feature at 6.64°E, 21.62°S is characterized by a domical hill and is best described as a tholus (Wangala Tholus). The tholus has an irregular basal shape that extends to its south and exhibits moderately sloping flanks. There are also prominent topographic rises that occur next to and around impact craters. Examples can be observed north of the rim of the Darzamat crater, around the Oltagon crater

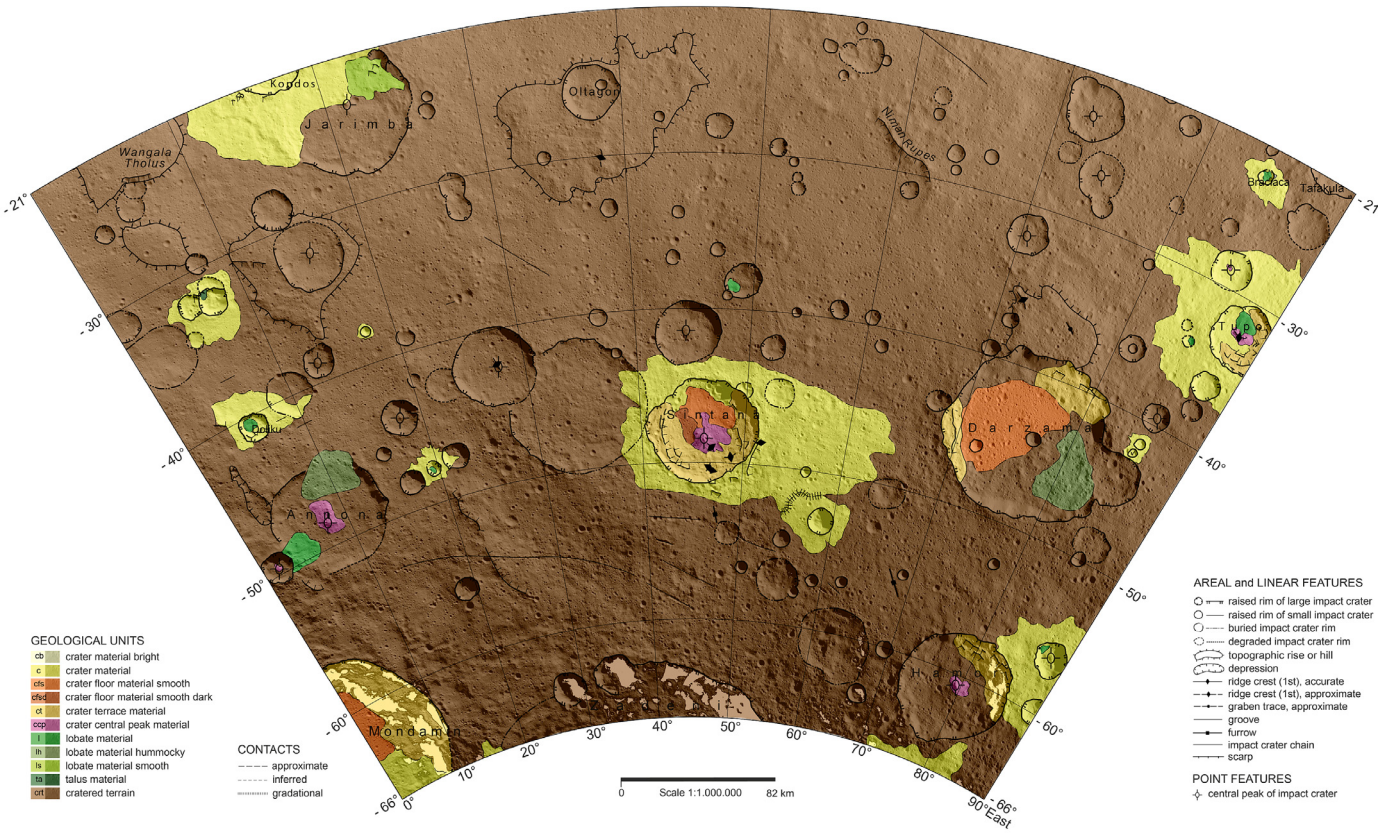

Fig. 5. Geologic map of the Ac-11 Sintana quadrangle on top of a clear filter LAMO mosaic. Units are displayed with a transparency of 50%. For a larger version of the map, we refer to the supplementary material.

(28 km, 37.96°E, 25.95°S) and around the 46-km large crater south of the Jarimba crater. Besides their variation in topography, they show no specific textures or colors (i.e., compositions).

Widespread crater chains also occur in the southern region of the Ac-11 Sintana quadrangle. Most of them are oriented SE-NW, while shorter chains with overall smaller craters occur all over the quadrangle with varying sense of direction. Some of the larger chain craters reveal crater rims that distinguish them from pit craters (Wyrick, 2004). Therefore, the crater chains are interpreted as secondary crater chains. There are two large scarps: Niman Rupes, and a less prominent scarp to the east of Annona crater. Those scarps are probably related to topography produced by ancient impacts. In addition, Tupo crater exhibits concentric fractures in its interior.

3.2. Map units

In the following sections we provide a description and interpretation of map units, which are displayed on the geologic map, as shown in Fig. 5.

3.2.1. Cratered terrain (crt)

Description: Cratered terrain is the dominant geologic unit of the quadrangle and exhibits the highest crater density with a variety of different crater preservation and degradation stages. All other units superimpose this one. The morphologies of ejecta blankets are highly subdued and erased by subsequent impacts and impact gardening.

Interpretation: Because of its crater density and the superimposition by younger units, the cratered terrain unit is interpreted to be the oldest unit of the quadrangle representing Ceres' ancient crust that is heavily degraded by ancient and recent impact events.

3.2.2. Crater materials (c, cb)

Description: The unit of cratered terrain is superimposed by different types of crater material that are deposited in and around craters with more distinctive fresh morphological features (e.g., sharper rims, preserved terraces, etc.). Continuous crater material units have been mapped, for instance, around Tupo crater and Kondos crater (44 km). Kondos' crater material covers large parts of the adjacent Jarimba crater (21.25°E, 24.08°S), which has a diameter of 69 km. High albedo crater material is mapped as bright crater material. The bright crater material (cb) appears mostly around extremely small craters. One example is the larger deposit surrounding the 8 km Braciaca crater at 84.4°E, 22.8°S. Crater material sometimes correlates with a higher F8/F3 ratio values (Fig. 4).

Interpretation: Crater material is interpreted as continuous ejecta blankets of relatively young impact craters. Morphologically it is mostly visible for fresh craters. One exception is the degraded Sintana crater. Bright crater materials are associated with ejecta blankets of very fresh impacts, which is supported by the high F8/F3 ratio values that characterize most of Ceres' young impact craters (Stephan et al., 2017b).

3.2.3. Lobate materials (l, lh, ls)

Description: Lobate material occurs as a positive relief feature and is deposited on a topographic gradient. Its deposition is always linked to a crater. It occurs in the craters Annona, Tupo, Darzamat, Jarimba and also in a few smaller ones (Fig. 5). The unit is classified into undivided (l), smooth (ls), and hummocky lobate material (lh). The classification mainly results from the degree of overprinting by craters. Smooth units have few overprinting craters. Hummocky units, on the other hand, exhibit many small craters on top. Undivided lobate material lies in between these two cases. Annona, for instance, shows a unit of undivided material (Fig. 6a). This unit

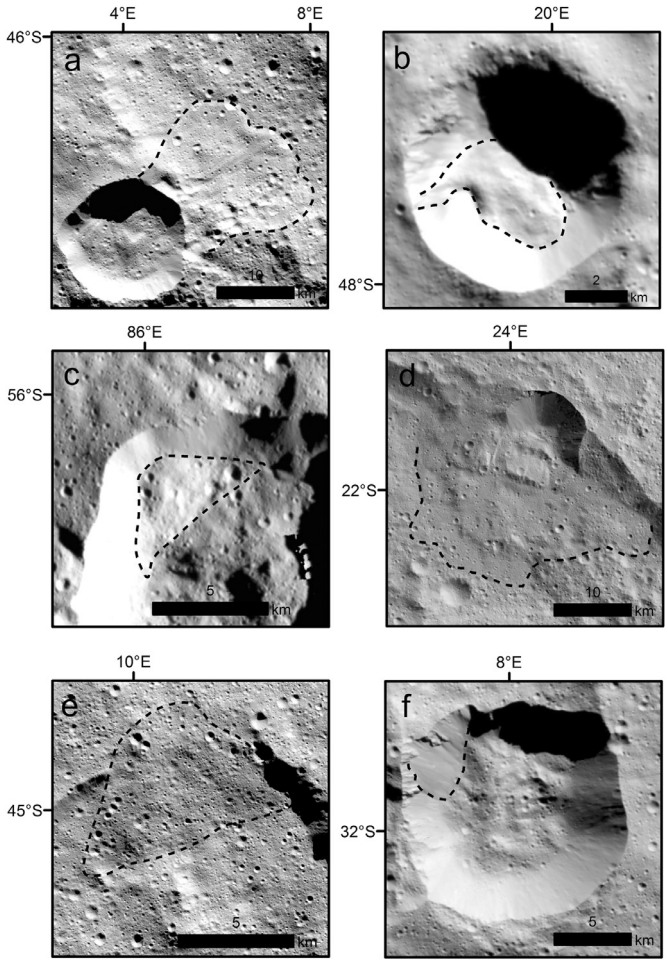

Fig. 6. Mass wasting features mapped as lobate (l, ls, lh) or talus material (ta) on clear filter mosaic images in LAMO resolution. (a) A lobate-shaped landslide in Annona mapped as undivided lobate material (l). The crater an Annona's crater rim from which the landslide emerges has a diameter of ~19 km. (b) A lobate shaped landslide in an unnamed crater mapped as undivided lobate material (l). (c) A blocky mass wasting feature mapped as undivided lobate material (l) in an unnamed crater(~18 km). (d) A landslide in Jarimba crater mapped as smooth lobate material (ls). (e) A mass wasting block in Annona mapped as humocky lobate material (lh) (f) and talus material (ta) inside an unnamed crater at 7.5°E, 32.3°S with a diameter of 16 km.

trends downslope, starting from a fresh crater on Annona's southeast crater rim, with maximum length of approx. 17 km and a maximum width of approx. 15 km. Two frontal lobes characterize its downslope front. Units of undivided lobate material (l) occur in different shapes ranging from lobate-shaped (Fig. 6b) to blocky in appearance (Fig. 6c). An example of a smooth lobate material unit occurs adjacent to the small impact crater (~15 km) on the northeast crater wall of Jarimba crater (69 km, 21.25°E, 24.08°S) (Fig. 6d), which has a particularly smooth surface texture. Annona also exhibits an example of hummocky lobate material with a rugged and chaotic surface structure (Fig. 6e), similar to a unit inside the 92 km Darzamat crater (76.4°E, 44.21°S).

Interpretation: The lobate material unit is interpreted to have been emplaced by mass wasting processes.

3.2.4. Smooth crater floor material (cfs, cfsd)

Description: Smooth crater floor material (Fig. 7a and b) occurs inside craters and is characterized by a low variation in topography. It is present in the craters Sintana (58 km), Mondamin (126 km) and Darzamat (92 km). Smooth crater floor material (cfs) always occurs on the lowermost floors of the craters. The interior of the Sintana (Fig. 7a and b) crater additionally contains a unit of dark smooth material (cfsd).

Interpretation: Smooth crater floor material is interpreted as impact melt (Schenk et al., 2016). Deposits of darker smooth crater floor material are interpreted as dark impact melt with a possibly different composition.

3.2.5. Crater terrace material (ct)

Description: Terrace material was mapped inside large complex craters, like Sintana (Fig. 7a and b) and Hamori (60 km). In most cases, only parts of the crater walls are terraced. There are always multiple terraces with varying widths concentric to the crater rim. Terrace material can have a smooth or hummocky texture. A type location for terrace material with a smooth surface structure is the southern interior of Sintana crater (Fig. 7a). A type location for terraced material with a more hummocky surface structure is, for instance, the western crater wall of Tupo crater (Fig. 6e).

Interpretation: Terrace material is a unit of mass wasting material, formed during the modification stage of the impact when the transient cavity collapses. Some parts of the terraces might have already been degraded.

3.2.6. Talus material (ta)

Description: Talus material is restricted to crater walls and is designated as fine material whose lineations suggest a downslope direction of movement. In the majority of cases, areas of talus material are too small to be mapped. One area of larger extent is located at a western slope of a young crater at 7.5°E, 32.3°S with a diameter of 16 km (Fig. 6f).

Interpretation: Talus material is interpreted to be debris of displaced material transported downslope due to slope instability. The texture of the mapped talus material suggests that it is composed of loosely consolidated materials.

3.2.7. Central peak material (ccp)

Description: The central peak material unit is used for topographically elevated areas in the approximate center of an impact crater. Sintana (Fig. 7a and b), Hamori, Annona have large central peaks and Tupo (Fig. 7e and f) has a central ridge. Central peak material is usually characterized by steep flanks, with slopes up to 25°. In the quadrangle area, central peaks are observed for craters larger than 15 km. In contrast, they are missing in several large craters, such as Darzamat and the crater west of Sintana.

Interpretation: Central peaks form during the crater's modification stage due to uplift (e.g. Melosh and Ivanov, 1999).

3.3. Highlighted craters

The Sintana quadrangle shows several complex craters, with different inner structures and features. Some particularly unique examples are discussed in the following sections.

3.3.1. Sintana crater

The 58-km crater Sintana (46.2°E, 48.07°S) is one of the largest craters in the quadrangle, and its collapsed interior formation and central peak are unique in this area. Sintana is located between two other large craters. Sintana is the morphologically youngest of the three craters with a large central peak (Fig. 7a). Flow fronts mark the termination of the crater material to the east (Fig. 2), which is interpreted to be the remnants of an ejecta blanket. The crater wall of the large degraded and thus older crater west of Sintana is buried, likely due to Sintana ejecta. Terraces have formed up to the actual rim of Sintana crater. The interior of the crater is characterized by multiple curved ridges and scarps (Fig. 7a and b). Concentric terraces stretch across the whole crater wall, except for the northern section. The southern crater floor is covered by

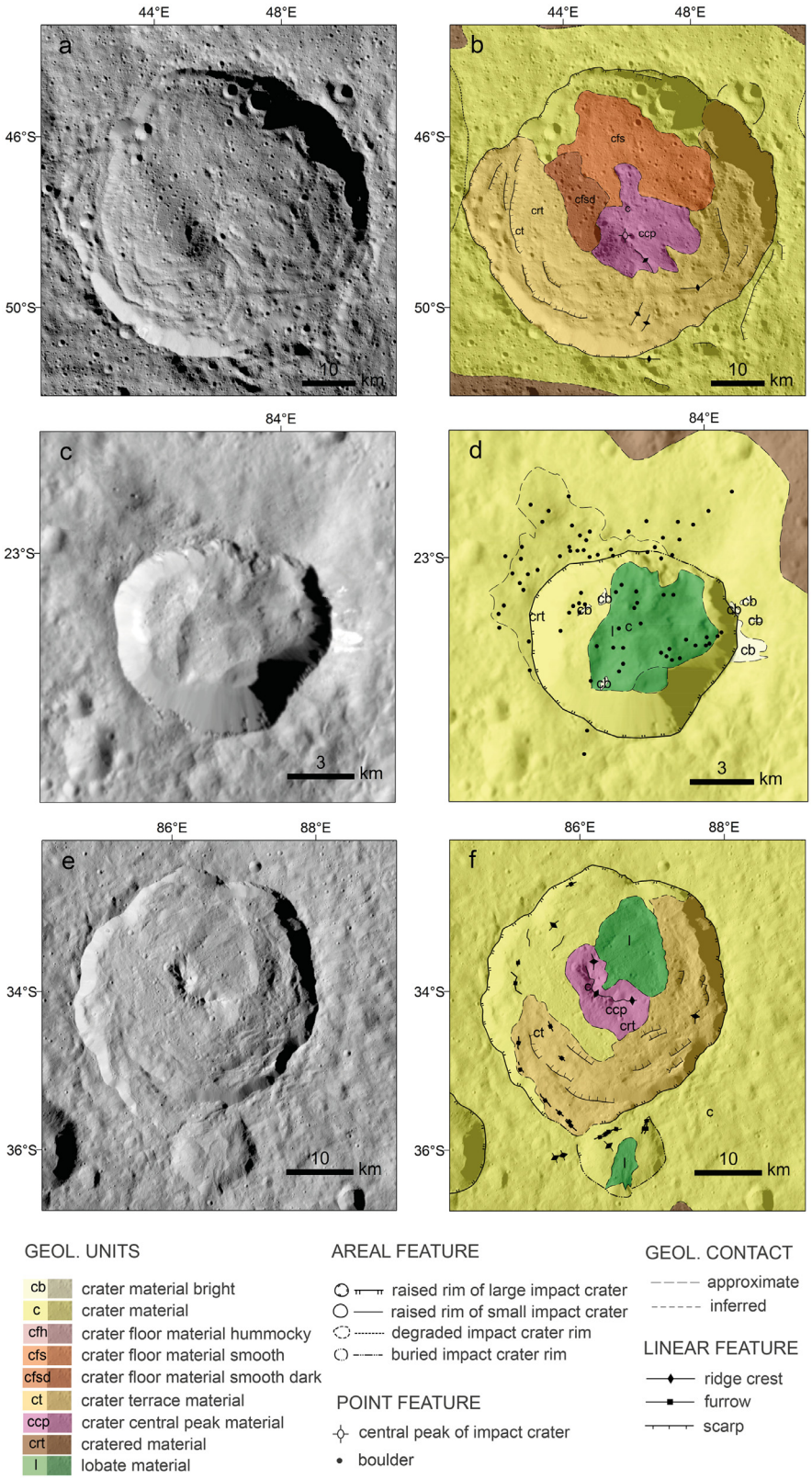

Fig. 7. Highlighted craters of the Sintana quadrangle with multiple inner crater structures. The craters are mapped in greater detail than the global map (Fig. 5). (a) LAMO clear filter image of Sintana crater. (b) Detailed map of Sintana crater. Several inner crater units were identified. (c) A LAMO-based clear filter image of Braciaca crater with rim deviated accumulated lobate material in the interior. (d) A detailed map of Braciaca crater's units and features. (e) LAMO clear filter image of Tupo crater. (f) Detailed map of Tupo crater including small-scale tectonic structures and peak deviated accumulated lobate material.

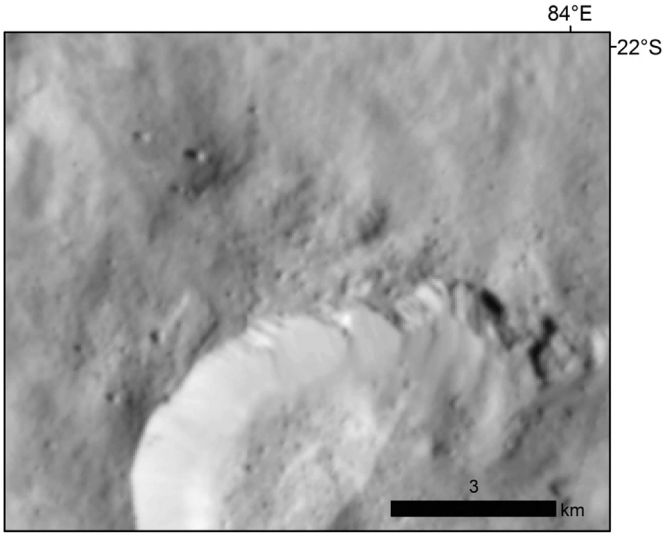

Fig. 8. A close-up showing the rich morphology of the northwestern part of Braciaca's ejecta blanket covered with boulders.

curved ridges. The closer they are to the crater center, the more radial is their orientation with respect to the crater center.

3.3.2. Braciaca crater

Braciaca crater (8 km in diameter) is located at 84.4°E, 22.8°S. It has one of the highest F8/F3 ratios in the quadrangle (Fig. 4). It is characterized by an irregular shape, a sharp crater rim, and steep crater walls (Fig. 7c and d). The interior of the Braciaca crater is filled with landslide deposits and appears spectrally red (Fig. 4).These landslides originated from several places at the northern and northwestern crater wall. Clear filter images reveal bright crater material to the east of the crater rim (Fig. 7c). Color ratios show an even more extensive ejecta layer with rays far beyond the morphologically visible part (Fig. 4). The visible ejecta to the north of the crater rim is much smoother than the parts to its south, which presumably is thinner, because small craters below the ejecta layer are still visible (Fig. 7c). Furthermore, there is a rough patch on the smooth ejecta deposit outside the northwest crater rim covered with many boulders (Fig. 8). Boulders also occur on the crater floor and on the lobate material inside the crater. Several dozen single boulders were identified with estimated diameters ranging from several tens to a few hundred meters. Boulders on Ceres are found to be predominantly clustered around craters with a fresh appearance (Schröder et al., 2016).

3.3.3. Tupo crater

Tupo crater (88.4°E, 32.3°S) has a diameter of 36 km and its morphology shows characteristics of a young complex crater because of its well-defined crater rim and pristine ejecta layer, which is clearly visible in clear filter images as well as in color ratios (Fig. 4). Tupo's complex interior exhibits an extensive, curved central ridge. The material around the central ridge is slightly smoother and brighter than the surrounding terrain. In addition to its widespread ejecta layer, Tupo crater features furrows at the outer edge of the crater floor that are concentric to the crater rim (Fig. 7e and f) and part of the crater's terraces. Additionally, there are several scarps that form extensive terraces, indicative of crater wall collapse that took place after the impact. The southeastern part of the terraced terrain is more hummocky than the southwestern part. Below Tupo's northeastern rim, there is a landslide that consists of a large block (Fig. 7e). It is mapped as lobate material. The block moved as a whole from the crater rim downslope as far as the central peak. The extent of its top is approximately 14 km. It lenses out downslope in contrast to explicitly lobate shaped landslides, such as in the Annona crater. A crater, about 13 km in diameter adjoins Tupo's southern crater rim. The rim of the smaller crater is not as well defined as Tupo's, because it is overlain by the Tupo ejecta of Tupo crater, which makes it stratigraphically older.

4. Geologic evolution

Fig. 9 contains the correlation of map units within the Sintana quadrangle. The relative chronostratigraphy has been derived from the observed superposition relations of geologic/geomorphological units supported by absolute age modeling (Figs. 10 and 11).

The oldest unit is the cratered terrain, because it is superposed by all other units. Crater counting provides an age of 1.1 ± 0.1 Ga with the LDM and 1.0 ± 0.3 Ga with the ADM, respectively (Fig. 10a). While the LDM fits the data much better at all crater diameters, the ADM allows the fit of two diameter ranges, because of the straight shape of the chronology function. The fit of larger diameters (~30-90 km) is in good agreement with the LDM-derived age. Fitting only the smaller diameters (~8-25 km) would yield a much younger age of 490 ± 60 Ma. The results of the randomness analysis (Fig. 10) show that the data values lie mostly within one standard deviation of the Monte Carlo-derived mean, therefore a random distribution of the counted craters can be inferred. Most of the ages that are reported for cratered terrain elsewhere on Ceres are older, ranging from 1.8 Ga (Platz et al., 2017) and 2 Ga (Williams et al., 2017b) up to 3.1 Ga (Pasckert et al., 2017). However, the age of the cratered terrain in the Sintana quadrangle is close to the age of ~1.3 Ga (LDM) and 0.2-0.9 Ga (ADM), as reported for the Kerwan smooth material that is interpreted as impact-induced melting of volatile, ice-rich crust (Williams et al., 2017b, this issue). The Kerwan impact (124°E, 11°S) is located to the northeast of the Sintana quadrangle. Based on the derived ages, we suggest that the Kerwan smooth material might have resurfaced the cratered terrain in the Sintana quadrangle. Parts in the north of the Sintana quadrangle were previously mapped as Kerwan smooth material on a global map using HAMO data (Mest et al., 2017). To test whether the young age of only the cratered terrain is restricted to a part of the quadrangle, we divided our counting area in two regions: the smaller region is the area that was mapped as Kerwan smooth material on the global map, and the remaining quadrangle area (Fig. 10b and c). We derived absolute ages of 1.2 ± 0.2 Ga (LDM) and 410 ± 50 Ma (using crater diameters of ~6–25 km) to 1.2 ± 0.3 Ga (using crater diameters of ~25-90 km) (ADM) for the southern region (Fig. 10b) and 1.1 ± 0.2 Ga (LDM) and 400 ± 80 Ma (ADM) for the possible resurfaced northern region of the quadrangle (Fig. 10c). The ages for the two subareas are close to the ones derived for the whole quadrangle. Thus, morphologic and ages estimates suggest that possible resurfacing events in the Sintana quadrangle were not restricted to specific areas.

Younger than the cratered terrain are several large degraded craters, such as Darzamat, Hamori and Annona. Their interior features, such as central peaks (ccp), terraces (ct), hummocky lobate material (lh) and smooth crater floors (cfs) are associated with the impact and crater modification. Consequently, those structures are nearly as old as their parent craters.

Sintana crater is the morphologically oldest crater that exhibits an ejecta blanket. The ejecta blanket is not as prominent as ejecta blankets of younger craters and is highly degraded. Most of the ejecta is mapped to the east of the crater. Another unit mapped only inside the Sintana crater is the dark smooth crater floor material (cfsd).

The morphologically youngest features in the Sintana quadrangle are the craters Kondos, Doliku, Tupo, Braciaca, and a few

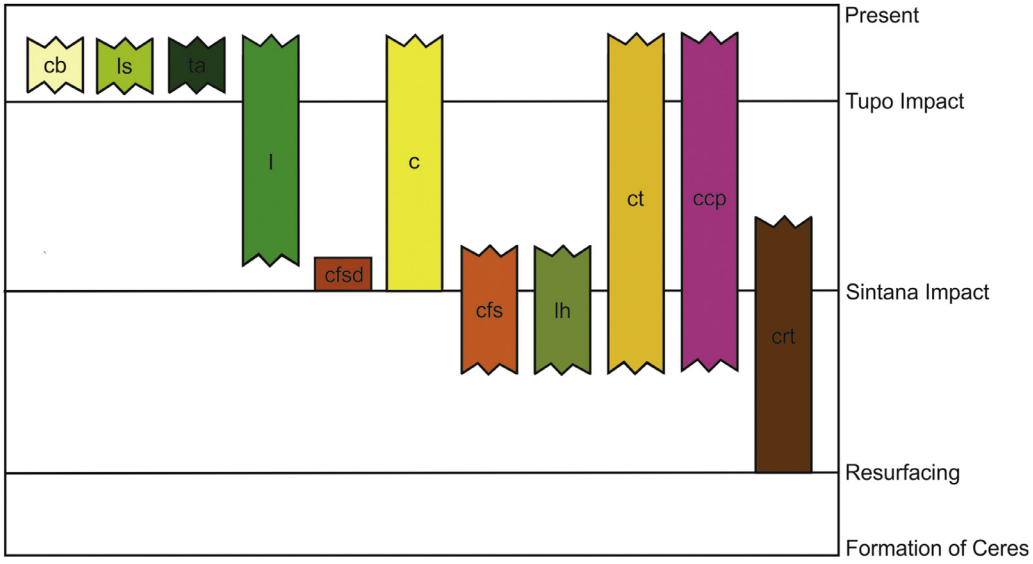

Fig. 9. Correlations of map units (COMU) for the Ac-11 Sintana quadrangle. Schematic axes classification.

smaller unnamed craters. In contrast to the other craters, only the ejecta blanket of Tupo is sufficiently broad to allow for reliable crater counts. It overprints all other units and shows no signs of secondary cratering, which is confirmed by the randomness analysis. The model age using the LDM is 29 Ma ± 2 and the ADM model age is 24 ± 2 Ma (Fig. 11). The LDM fits the data more exactly, especially in the larger diameter range. The randomness analysis gives values up to ±3 standard deviations from the Monte Carlo-derived mean, which is still considered to be most likely random. The 8-km Braciaca crater is characterized by a fresh morphology, such as a distinct crater rim. Parts of its ejecta blankets are bright in clear filter images. It also has one of the highest F8/F3 ratios in the quadrangle, indicative of a young absolute age. Fig. 12 illustrates the correlation of the ejecta blankets of the fresh craters Tupo and Braciaca correlate with a high F8/F3 color ratio. By comparing color ratios F8/F3 and F8/F5 (365 nm) with absolute age measurements, Schmedemann et al. (2016) found that model ages increase with decreasing color ratio. The spectral analysis also shows that a smaller 2.7 band mostly correlates with morphologically young features (De Sanctis et al., 2017a). These correlations have been interpreted to be associated with changes in the physical properties of the unweathered surface material or as a result of the impact event (De Sanctis et al., 2017b; Stephan et al., 2017a). Those changes diminish with increasing surface age due to surface processes such as space weathering (Stephan et al., 2017b). Units that occur inside young craters are talus material (ta) and smooth and (undivided) lobate.

5. Discussion

The Ac-11 Sintana quadrangle of Ceres is mapped as part of the Dawn global geological analysis. Local features, such as craters, their morphology and deposits, and landslides were compared with similar ones on Ceres in order to understand how the Sintana quadrangle fits into the global geologic evolution. In addition, we estimate how tectonics and volcanic activity that have been identified in other regions on Ceres are relevant for the studied area in the southern hemisphere. For this purpose, gray-scale images, supported by topographic and color data of the Sintana quadrangle were used.

Absolute ages suggest that the Sintana quadrangle experienced a quadrangle-wide resurfacing by Kerwan impact melt, although distinct morphological deposits could not be identified. The north and south of the quadrangle show no difference in absolute age estimates. In contrast, spectral mapping of the Sintana and more eastern Toharu quadrangle reveals an increase in phyllosilicate and ammoniated phyllosilicate band intensity to the south of both quadrangles. This trend loosely coincides with topography, but is interpreted as the result of compositional heterogeneities in the Cerean crust (De Sanctis et al., 2017a). However, the age data indicate a possible significant influence of the Kerwan smooth material that might have affected at least the northern but more likely the whole quadrangle area. The less heavily cratered southern hemisphere of Ceres is associated with large impact events, such as Urvara and Yalode (Hiesinger et al., 2016), which could also have overprinted the Sintana quadrangle. However, the larger distances and reported absolute ages for the Yalode basin (580 ± 40 Ma, LDM) and Urvara basin (550 ± 50 Ma, LDM) by Crown et al. (2017), which are younger than the material that fills and surrounds the Kerwan basin and the cratered terrain in the Sintana quadrangle, indicate that impact-induced melting from Kerwan impact is the quadrangle's most important resurfacing influence.

The features mapped in the Sintana quadrangle, such as crater shapes from highly degraded to fresh, landslides, secondary crater chains and concentric fractures, are typical for Ceres (Buczkowski et al., 2016). Craters in the Sintana quadrangle do not show pitted crater floors as observed for Haulani and Ikapati, which are interpreted to be an indicator for volatile-rich material deposited in such craters (Krohn et al., 2016; Sizemore et al., 2017).

Some large craters, such as the 80-km crater to the west of Sintana at 34.09°E, 45.62°S, do not have central peaks, while other craters of the same size in the quadrangle do contain central peaks. There could be several explanations for missing central peaks in large craters in the Sintana quadrangle. It has been postulated that viscous relaxation is limited to just some shallow craters indicating a spatially varying subsurface (Bland et al., 2016). Viscous relaxation is a wavelength-dependent change in topography. Long-wavelength topography is affected much more than short-wavelength topography (Hall et al., 1981). This effect would therefore lead to shallower craters, but with rims and central peaks that are still recognizable. Therefore this model cannot fully explain the absence of central peaks in the quadrangle. Another effect could be the burial of the peak by mass-wasting material. A burial by lava that floods the crater floor, similar to what is observed for lunar craters (Pike, 1971), seems unlikely, even if cryovolcanism is con-

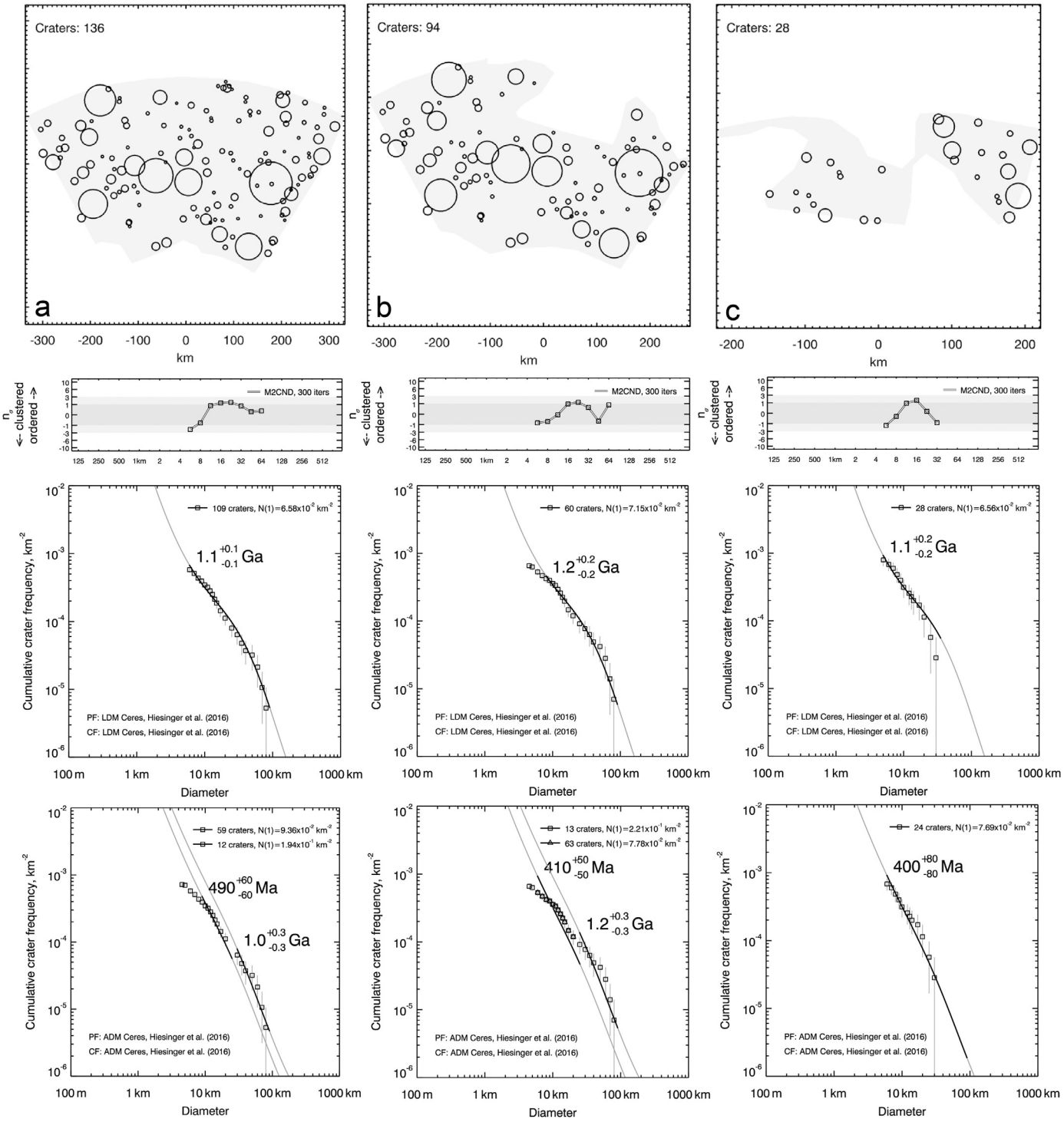

Fig. 10. Crater size-frequency distributions and best-fit model ages for the cratered terrain (crt). (a) Craters > 5 km with their center in the Sintana quadrangle were used to determine an absolute age for the quadrangle-wide area. The upper image shows the counting area with all counted craters. Below, the results of the randomness test and the best-fit model ages using the LDM and the ADM. (b) Absolute ages using craters > 5 km were estimated for the southern region of the quadrangle. The region that is supposingly overprinted by the Kerwan smooth material is left out. The upper image shows the counting area with all counted craters. Below, the results of the randomness test and the best-fit model ages using the LDM and the ADM. (c) Absolute ages were estimated for the region that possibly was resurfaced by the Kerwan smooth material. The upper image shows the counting area with all counted craters. Below, the results of the randomness test and the best-fit model ages using the LDM and the ADM.

sidered for some features on Ceres (e.g. Krohn et al., 2016; Ruesch et al., 2016). The peaks might also have been destroyed by impact gardening, like what possibly occurred inside Darzamat crater, which has a small crater instead of a peak in its approximate center. Some large complex craters undergo modifications that lead to peak-ring craters. This transition is either explained by central peak collapse (e.g. Collins et al., 2002; Morgan et al., 2016) or by the nested melt-cavity model (Baker et al., 2011; Head, 2010). We find no peak-ring craters in our quadrangle, but those large craters without central peaks might have experienced a transition, even if it has not been completed.

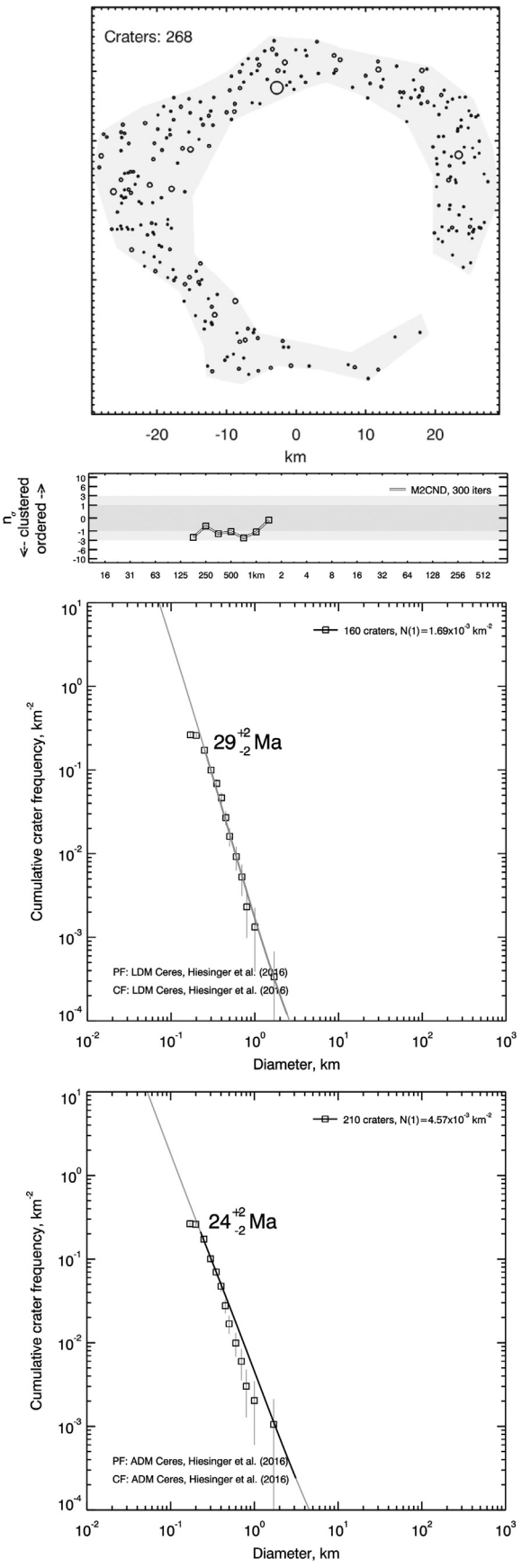

Fig. 11. Age determination for Tupo crater. The upper image shows the counting area with all counted craters. The results of the randomness test, the crater size-frequency distribution and the best-fit model ages (LDM and ADM) are displayed below. Only craters > 200 m were used for the fit.

Landslides in the Sintana quadrangle resemble features on other planetary bodies. Landslides that are most likely triggered by small impacts on crater rims are also observed on other small Solar System objects, such as Lutetia (e.g., Thomas et al., 2012). Numerical investigations by Elbeshausen et al. (2012) suggest that the localization and style of a landslide on asteroid (21) Lutetia, similar to the ones identified on Ceres, result from weakening due to acoustic fluidization caused by the impact process. Alternatively, blocky landslides were probably caused by a rotational slumping process. Some blocky landslides, such as the huge block inside Tupo (Fig. 7e), are similar to Toreva block landslides on Earth, which originate when a stronger unit collapses as a nearly intact block after the underlying weaker unit erodes (Melosh, 2011; Reiche, 1937). The landslide inside the Braciaca crater has a lower color ratio than the ejecta blanket of the crater. The mass wasting process probably transported older material into the crater, overlaying the young fall-back material deposits on the crater floor. This is similar to the 20-km Juling crater on Ceres at 168.4°E, 35.9°S (Stephan et al., 2017a).

Some landslides, mapped as undivided and smooth lobate material (Fig. 6a, b, d), correlate with identified flow features that are associated with ground ice (Schmidt et al., 2017). The three flow types described in Schmidt et al. (2017) have morphologies and aspect ratios that are more similar to ice-rich flows than to dry landslides. The undivided and smooth lobate material in the Sintana quadrangle are comparable to the type of flow described by Schmidt et al. (2017) as a long run-out landslide with circular to lobate toes.

The Sintana quadrangle lacks features that are related to volcanic activity. Hiesinger et al. (2016) identified several low crater density terrains on Ceres. Most of those areas are interpreted to have been formed by resurfacing. One of such areas in the Sintana quadrangle centered at 54.2°E/23.3°S, may have an endogenic origin as it displays features, such as dome-like structures and graben-like valleys and nested pits (Hiesinger et al., 2016). We, however, interpret possible dome-like structures as small variations in topography, probably related to impacts in this area. The resolution limits the distinction between pits and (secondary) craters. Tholi on Mars are of volcanic origin and show structures, such as channels, troughs and caldera pits (e.g. Plescia, 2004; Werner, 2009). In the Sintana quadrangle, tholi only differ topographically from surrounding terrain without morphological or compositional evidence for volcanic activity (Platz et al., 2015) or uplifting by diapirism or shallow intrusions (Fagents, 2003; Ruesch et al., 2016). They may be impact related remnants or part of the pre-impact surface, but are no evidence for an active interior of Ceres within the Sintana quadrangle.

Linear structures are interpreted to be secondary crater chains or impact-related structures, such as concentric fractures in Tupo, similar to fractures in Occator and Dantu, which are interpreted to be the result of cooling-melting processes or the sinking of the crater floor (Buczkowski et al., 2016; von der Gathen et al., 2016). We suggest that the specific arrangement of ridges inside the Sintana crater is the result of a converging motion of terraces, similar to radial transpression ridges in craters described by Kenkmann and Dalwigk (2000) that are formed to compensate centro-symmetric motion of masses during the gravity-collapse of the crater, as illustrated in Fig. 13.

The mapping process is restricted by the limit of resolutions, especially for linear structures. A clear distinction between impact-generated secondary craters or tectonically generated pit craters cannot be drawn with absolute certainty. Additionally, there are a few image gaps in the mosaics, and unfavorable illumination conditions (shadows) towards the South Pole. Due to a high occurrence of secondary craters, we restricted age estimates to two units: the cratered terrain, by only using craters larger than 5 km,

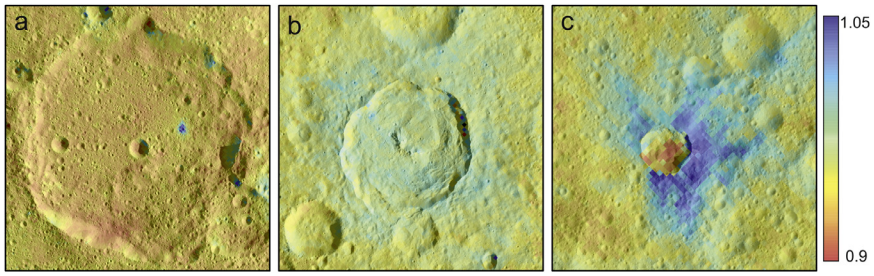

Fig. 12. Color ratio F8/F3 (60% transparency) on top of a clear filter mosaic for the craters Darzamat (a), Tupo (b) and Braciaca (c). The color ratio is increasing with decreasing age. The old degraded Darzamat crater has a lower F8/F3 color ratio than the younger Tupo and Braciaca craters. A very small impact inside Darzamat crater shows a high color ratio as well. In the Sintana quadrangle, Tupo is the largest crater with a high F8/F3 color ratio. In other regions of Ceres, there are also large craters, such as Haulani and Occator that are characterized by a higher ratio (Stephan et al., 2017b).

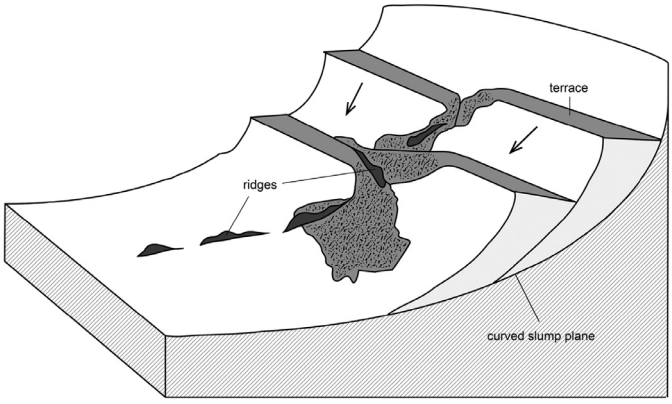

Fig. 13. Schematic illustration of two colliding terrace bundles in the southern part of Sintana crater. Collision results in radial ridges and chaotic slumps and landslides.

and Tupo ejecta as a low overprinted counting area. Besides contamination with secondary craters, there is a systematic error due to uncertainties in both production and chronology function and their interaction, and also the statistical error (Michael and Neukum, 2010).

6. Conclusion

Absolute age estimates suggest that the Sintana quadrangle was overprinted, possibly by the same material that fills and surrounds the Kerwan impact basin, and therefore is less heavily cratered than other regions of Ceres' surface. Endogenic activity is not observed for this region of Ceres because there is a lack of morphologically distinct volcanic landforms and related tectonic structures. The absence of such structures might be due to the resurfacing by impact-induced melting or different interior conditions in this area of Ceres that might be related to a thicker crust or different temperature conditions in the interior. Identified mass wasting features support an ice-rich subsurface composition.

Acknowledgments

We thank guest editor Michael Bland, Nadine G. Barlow and two anonymous reviewers for their helpful comments and reviews of our paper. Additionally, we thank the Dawn team for the development, cruise, orbital insertion, and operations of the Dawn spacecraft at Ceres. Dawn data are archived with the NASA Planetary Data System (http://sbn.pds.nasa.gov/).

Supplementary materials

Supplementary material associated with this article can be found, in the online version, at doi:10.1016/j.icarus.2017.12.007.

References

Baker, D.M.H., et al., 2011. The transition from complex crater to peak-ring basin on Mercury: new observations from MESSENGER flyby data and constraints on basin formation models. Planet. Space Sci. 59, 1932–1948.
Bland, M.T., 2013. Predicted crater morphologies on Ceres: probing internal structure and evolution. Icarus 226, 510–521.
Bland, M.T., et al., 2016. Composition and structure of the shallow subsurface of Ceres revealed by crater morphology. Nat. Geosci 9, 538–542.
Buczkowski, D.L., et al., 2016. The geomorphology of Ceres. Science 353, aaf4332.
Castillo-Rogez, J.C., McCord, T.B., 2010. Ceres' evolution and present state constrained by shape data. Icarus 205, 443–459.
Collins, G.S., Melosh, H.J., Morgan, J.V., Warner, M.R., 2002. Hydrocode simulations of chicxulub crater collapse and peak-ring formation. Icarus 157, 24–33.
Crown, D.A., et al., 2017. Geologic mapping of the Urvara and Yalode Quadrangles of Ceres. Icarus this issue.
De Sanctis, M.C., et al., 2011. The VIR spectrometer. Space Sci. Rev. 163, 329–369.
De Sanctis, M.C., et al., 2017a. Ac-H-11 Sintana and Ac-H-12 Toharu quadrangles: assessing the large and small scale heterogeneities of Ceres' surface. Icarus. in press.
De Sanctis, M.C., et al., 2017b. Ac-11-Sintana and Ac-H-12 Toharu quadrangles: assessing the large and small scale heterogeneities of Ceres' surface. Icarus. in press.
Elbeshausen, D., Wünnemann, K., Sierks, H., Vincent, J.B., Oklay, N., 2012. Landslides triggered by impacts on asteroid (21) Lutetia? In: EPSC 2012, p. 673. (abstract).
Ermakov, A.I., et al., 2017. Constraints on Ceres' internal structure and evolution from its shape and gravity measured by the Dawn spacecraft. J. Geophys. Res.: Planets 122.
Fagents, S.A., 2003. Considerations for effusive cryovolcanism on Europa: the post–Galileo perspective. J. Geophys. Res.: Planets 108, 5139.
Fu, R.R., et al., 2017. The interior structure of Ceres as revealed by surface topography. Earth Planet. Sci. Lett. 476, 153–164.
Hall, J.L., Solomon, S.C., Head, J.W., 1981. Lunar floor-fractured craters: evidence for viscous relaxation of crater topography. J. Geophys. Res.: Solid Earth 86, 9537–9552.
Head, J.W., 2010. Transition from complex craters to multi-ringed basins on terrestrial planetary bodies: Scale-dependent role of the expanding melt cavity and progressive interaction with the displaced zone. Geophys. Res. Lett. 37, L02203.
Hiesinger, H., et al., 2016. Cratering on Ceres: implications for its crust and evolution. Science 353, aaf4759.
Kenkmann, T., Dalwigk, I., 2000. Radial transpression ridges: a new structural feature of complex impact craters. Meteorit. Planet. Sci. 35, 1189–1201.
Kneissl, T., van Gasselt, S., Neukum, G., 2011. Map-projection-independent crater size-frequency determination in GIS environments—new software tool for ArcGIS. Planet. Space Sci. 59, 1243–1254.
Konopliv, A.S., et al., 2011. The Dawn gravity investigation at Vesta and Ceres. Space Sci. Rev. 163, 461–486.
Krohn, K., et al., 2016. Cryogenic flow features on Ceres: implications for crater-related cryovolcanism. Geophys. Res. Lett. 43, 11994–12003.
Marchi, S., et al., 2016. Cratering on Ceres: the puzzle of the missing large craters. Lunar Planet. Sci. XXXXVII, 1281 (abstract).
McCord, T.B., Sotin, C., 2005. Ceres: evolution and current state. J. Geophys. Res. 110, E05009.
Melosh, H., Ivanov, B., 1999. Impact crater collapse. Annu. Rev. Earth Planet. Sci. 27, 385–415.
Melosh, H.J., 2011. Planetary Surface Processes. Cambridge University Press.
Mest, S., et al., 2017. The global geologic map of Ceres based on Dawn HAMO observations. In: 48th Lunar Planet. Sci. Conf. Lunar and Planetary Institute. The Woodlands, p. 2512.
Michael, G.G., 2013. Planetary surface dating from crater size-frequency distribution measurements: multiple resurfacing episodes and differential isochron fitting. Icarus 226, 885–890.
Michael, G.G., Neukum, G., 2010. Planetary surface dating from crater size-frequency distribution measurements: partial resurfacing events and statistical age uncertainty. Earth Planet. Sci. Lett. 294, 223–229.

Michael, G.G., Platz, T., Kneissl, T., Schmedemann, N., 2012. Planetary surface dating from crater size–frequency distribution measurements: spatial randomness and clustering. Icarus 218, 169–177.
Morgan, J.V., et al., 2016. The formation of peak rings in large impact craters. Science 354, 878.
Naß, A., et al., 2015. GIS-based template for geological mapping - Ceres use case. In: Conference Proceedings. ISPRS Workshop of Working Group IV/8: Planetary Mapping and Spatial Databases.
Naß, A., van Gasselt, S., Jaumann, R., Asche, H., 2011. Implementation of cartographic symbols for planetary mapping in geographic information systems. Planet. Space Sci. 59, 1255–1264.
Park, R.S., et al., 2016. A partially differentiated interior for (1) Ceres deduced from its gravity field and shape. Nature 537, 515–517.
Pasckert, J.H., et al., 2017. Geologic mapping of the Ac-2 Coniraya quadrangle of Ceres from NASA's Dawn mission: implications for a heterogeneously composed crust. Icarus. this issue.
Pike, R.J., 1971. Genetic implications of the shapes of martian and lunar craters. Icarus 15, 384–395.
Platz, T., et al., 2015. Putative volcanic landforms on Ceres. In: EPSC 2015, p. 915. (abstract).
Platz, T., et al., 2017. Geological mapping of the Ac-10 Rongo quadrangle of Ceres. Icarus. this issue.
Plescia, J.B., 2004. Morphometric properties of Martian volcanoes. J. Geophys. Res. 109, E03003.
Prettyman, T.H., et al., 2011. Dawn's gamma ray and neutron detector. Space Sci. Rev. 163, 371–459.
Preusker, F., et al., 2016. Dawn at Ceres – shape model and rotational state. Lunar Planet. Sci. XXXXVII, 1954 (abstract).
Reiche, P., 1937. The Toreva-block: a distinctive landslide type. J. Geol. 45, 538–548.
Roatsch, T., et al., 2016. High-resolution Ceres high altitude mapping orbit atlas derived from Dawn framing camera images. Planet. Space Sci. 129, 103–107.
Ruesch, O., et al., 2016. Cryovolcanism on Ceres. Science. 353.
Russell, C.T., Raymond, C.A., 2011. The Dawn mission to Vesta and Ceres. Space Sci. Rev. 163, 3–23.
Schenk, P.M., et al., 2016. Impact cratering on the small planets Ceres and Vesta: S-C transitions, central pits, and the origin of bright spots. Lunar Planet. Sci. XXXXVII, 2697 (abstract).
Schmedemann, N., et al., 2016. Timing of optical maturation of recently exposed material on Ceres. Geophys. Res. Lett. 43, 11987–11993.
Schmidt, B.E., et al., 2017. Geomorphological evidence for ground ice on dwarf planet Ceres. Nat. Geosci 10, 338–343.
Schröder, S.E., et al., 2016. Boulders on Ceres. EGU (abstract).
Shoemaker, E.M., 1965. 2. Preliminary analysis of the fine structure of the lunar surface in mare cognitum. Int. Astron. Union Colloq. 5, 23–77.
Sierks, H., et al., 2011. The Dawn framing camera. Space Sci. Rev. 163, 263–327.
Sizemore, H.G., et al., 2017. Pitted terrains on (1) Ceres and implications for shallow subsurface volatile distribution. Geophys. Res. Lett. 44, 6570–6578.
Stephan, K., et al., 2017a. An investigation of the bluish material on Ceres. Geophys. Res. Lett. 44, 1660–1668.
Stephan, K., et al., 2017b. Ceres' craters – relationships between surface composition and geology. Icarus. in press.
Thomas, N., et al., 2012. The geomorphology of (21) Lutetia: results from the OSIRIS imaging system onboard ESA's Rosetta spacecraft. Planet. Space Sci. 66, 96–124.
USGS, 2006. FGDC digital cartographic standard for geologic map symbolization (postscript implementation): U.S. Geological Survey Techniques and Methods 11-A2.
von der Gathen, I., et al., 2016. Deformational features on Ceres' surface compared to other planetary bodies. Lunar Planet. Sci. XXXXVII, 1961 (abstract).
Werner, S.C., 2009. The global Martian volcanic evolutionary history. Icarus 201, 44–68.
Williams, D.A., Buczkowski, D.L., Mest, S.C., Scully, J.E.C., Thomas, P., Thomas, K., 2017a. Introduction: the geologic mapping of Ceres. Icarus. this issue.
Williams, D.A., et al., 2017b. The geology of the Kerwan quadrangle of dwarf planet Ceres: investigating Ceres' oldest, largest impact basin. Icarus. this issue.
Williams, D.A., Yingst, R.A., Garry, W.B., 2014. Introduction: the geologic mapping of Vesta. Icarus 244, 1–12.
Wyrick, D., 2004. Distribution, morphology, and origins of Martian pit crater chains. J. Geophys. Res. 109, E06005.
Yingst, R.A., et al., 2014. Geologic mapping of Vesta. Planet. Space Sci. 103, 2–23.